A fast evaluation method for fatigue strength of maraging steel: The minimum strength principle

Z.K. Xu [a, b], B. Wang [b, c], P. Zhang [a, b, c*] and Z.F. Zhang [a, b, c*]

[a] *School of Materials Science and Engineering, University of Science and Technology of China, Hefei 230026, China*

[b] *Laboratory of Fatigue and Fracture for Materials, Institute of Metal Research, Chinese Academy of Sciences, Shenyang 110016, China*

[c] *Jihua Laboratory, Foshan 528200, China*

Abstract

The relationship between fatigue strength and tensile properties has drawn widespread concern in recent decades. It is gradually recognized that the fatigue strength is dependent on the strength of the weakest zone in materials, while the regular tensile test could only obtain the global strength. The present study, for the first time, constructed a fast evaluation method, in which extremely slender specimens were employed. It is found that, when the specimen is slender enough, i.e., the soft oriented grain could occupy the whole section of the specimen, the strength of the soft domain could be related to the fatigue strength. In the 18Ni maraging steels, the fatigue crack would nucleate in the precipitate free zone (PFZ), which is the soft domain. Furthermore, the fatigue strength of fully reversed loading test nearly equals to the yield strength of the PFZ measured by the slender tensile test. This founding may shed light on the fast evaluation of fatigue strength, which could bring great economic benefits and save invaluable time.

Keywords: Maraging steel; Fatigue strength; Fatigue crack initiation; Yield behavior; Deformation inhomogeneity.

* Corresponding author. E-mail: pengzhang@imr.ac.cn (P. Zhang), zhfzhang@imr.ac.cn (Z.F. Zhang).

1. Introduction

Fatigue is referred to as the damage and failure of materials under cyclic loading. Nowadays, the fatigue strength has already become an essential index for structural materials selection. However, the fatigue tests to measure the fatigue strength would take a lot of money and time. Therefore, many research efforts have been devoted to relating the fatigue strength to mechanical properties that are easy to obtain, such as the ultimate tensile strength (UTS) [1, 2]. In the 1870s, Wöhler firstly found that the fatigue strength and UTS followed a simple linear relation [1]. Recently, it has been found that the high-strength steels do not follow this linear rule [2-4]. Therefore, Pang et al. proposed a parabolic relation between the fatigue strength and UTS [2]. However, those relations are mostly summarized from the experimental data. The parameters in Pang's formula obtained by fitting have no clear physical meanings. Therefore, they will change when it comes to different materials or different fatigue damage mechanisms, which are difficult to predict before knowing the fatigue property. Hence, it is significantly important to establish a method to evaluate the fatigue strength quickly by taking into account the fatigue damage mechanisms in detail.

For most general cases, the evolution of fatigue damage can be broadly categorized into the following stages: 1) microstructural changes leading to the nucleation of permanent damage; 2) the formation of microscopic cracks; 3) the growth of microscopic cracks to dominant crack; 4) stable propagation of the dominant crack; 5) final failure [5-7]. A significant fraction of research effort has been devoted to the study about the effect of the microstructure on the first two stages. According to the sources of fatigue damage, the conclusions can be divided into the following items. Firstly, the fatigue crack generally nucleates from the stress concentration positions, such as microscopic flaws, inclusions and pores [8, 9]. Secondly, the fatigue crack often nucleates from the soft domain, such as the secondary phase, and the precipitate-free zone [4, 10]. Even for those materials without metallurgical defects, the microstructural inhomogeneity exists commonly. Several instances can be listed as follows. Firstly, in the polycrystalline metals, the soft oriented grains would be generally the soft domain [11]. Secondly, abnormal large grains produced by partial recrystallization during cold

rolling and tempering would induce the microstructural inhomogeneity according to the Hall-Petch relationship [12-14]. Thirdly, different phases have different strengths in the multiphase metals, such as the ferrite/martensite duplex steels [10, 15, 16] and the alpha/beta titanium alloys [17]. Fourthly, the attendance of the precipitate-free zone (PFZ) in the aging strengthening materials would generate the microstructural inhomogeneity, particular among the aluminum alloys, titanium alloys and maraging steels [4, 18-20]. In a word, there is always a relatively soft domain in the materials, which is the preferred site for fatigue cracking.

In general, the crack would appear first in the soft domain for metals without metallurgical defects under cyclic loading [12, 18-20], which means that the fatigue strength is mainly determined by the local strength of the soft domain. Liu et al. reported that abnormal large grains produced by partial recrystallization would nucleate fatigue crack first due to the relatively low strength compared to the fine grain domain and the fatigue strength approximately equals to the yield strength of the large grain [12, 21]. The possibility exists that the yield strength of the large grain could be detected by the microhardness test. However, the microhardness test of the lamellar shaped soft domains, such as PFZ in the precipitation strengthening materials, would face challenges. Lütjering et al. reported that the PFZ would deform preferentially under cyclic loading in high-strength aluminum alloys and beta titanium alloys, which had a strong influence on fatigue strength [20]. In that study, a minimum fatigue strength of maraging steel occurs when the PFZ appeared at an angle of 45° to the loading direction, which produced the maximum shear stress [20]. Because the PFZ has great influence on the fatigue property, a new evaluation method to detect the strength of PFZ is required. Here, we will introduce our ideas as follows.

Similar to the performance of the soft domain in high-cycle fatigue (HCF), the soft domain would also start the dislocation slip first during monotonic tension [22], merely it would not nucleate crack immediately. When achieving the yield strength of the soft domain, the surrounding hard domains remain elastic so that the soft domain cannot deform freely until the hard domain matrix yields [22]. However, as for cyclic loading,

when the maximum stress achieves the yield strength of the soft domain, the tiny plastic deformation would accumulate due to the slip irreversibility leading to the nucleation of microcrack [6]. That is to say, the tensile test could only obtain the global yield strength of materials, while the fatigue strength is mainly dependent on the yield strength of the local soft domain. But the conclusion above is only based on the traditional tensile specimen. Things might become different if the tensile specimen could be manufactured extremely slender to the extent that a single soft grain could occupy the whole section of the specimen. Therefore, the soft domain could deform freely and such a tensile test might be able to measure the yield strength of the soft domain.

In the present study, some extremely slender tensile specimens were manufactured, and the differences of deformation behaviors between the slender and the regular specimens were carefully investigated. The damage mechanism of the slender specimens was revealed and the relationship between the yield strength and fatigue strength for the two kinds of specimens was established.

2. Experimental procedures

2.1. Materials fabrication

18Ni Co-free maraging steel was employed in this study, of which the elemental compositions were obtained by the chemical analysis and the results were shown in Table 1. Some bars were cut from the as-received hot forged plate, and then were solution heat treated at 850 °C for 1 h, followed by the water-quench and aging treatment. The aging treatments used in the present study were 500 °C for 5 h, 550 °C for 5 h, 600 °C for 3 h and 630 °C for 3 h, respectively.

Table 1 Elemental compositions of the experimental maraging steel (wt.%).

Ti	Cr	Mo	Ni	Si	Mn	P	S	C	Fe
1.55	0.21	3.24	18.4	0.07	<0.005	<0.005	<0.003	<0.02	Bal.

The metallographic samples were cut from the bars after aging treatment, then electropolished at a voltage of 21 V in a solution of 10% $HClO_4$ and 90% CH_3COOH

for 40 seconds at room temperature. The microstructures of the samples under different aging treatments were observed by SUPRA 35 scanning electric microscope (SEM), with a working distance of 12 mm, and the detector of Inlens. The distributions of elements were detected by the energy-dispersive X-ray spectroscopy (EDS) with the Octane Elite EDS System, of which the detector incorporated a new silicon nitride (Si_3N_4) window, operated at the accelerating voltage of 20 kV and the working distance of 9.6 mm.

2.2. Slender tensile tests

The preparation of the slender tensile (ST) specimens consisted of several steps. Firstly, the specimen was cut off from the aged bar by the wire cut electrical discharge machining (WEDM) and sanded to remove the rough surface caused by WEDM. Since the specimen is too flexible, the whole specimen needs to be supported when the side was being sanded. Then we used a piece of plasticine to accomplish that task. After the sanding, the section of the specimen is about 200×200 μm^2. Secondly, the dimension reduction of the section of the specimen was allotted to the electrochemical etching method. A home-made device was set up to implement the electrochemical etching machining and to control the dimension of the specimen through the compliance method. The device had two main modules: the electrochemical etching module and the compliance measurement module. The composition of the etching solution was 10% $HClO_4$ and 90% CH_3COOH and the supply voltage was 6 V. As for the compliance of the specimen, it was caused by its own gravity when the specimen was put into incline. When the real-time compliance reached the target value that was calculated using the target specimen configuration dimension as shown in Fig. 1a, the electrochemical etching was ceased manually. Then the specimen was cleaned by ultrasonic with alcohol. The final specimen and the testing process can be seen in Figs. 1b and 1c, respectively. The ST tests were carried out on the MMT110N testing machine at a strain rate of 5×10^{-4} s^{-1} at room temperature.

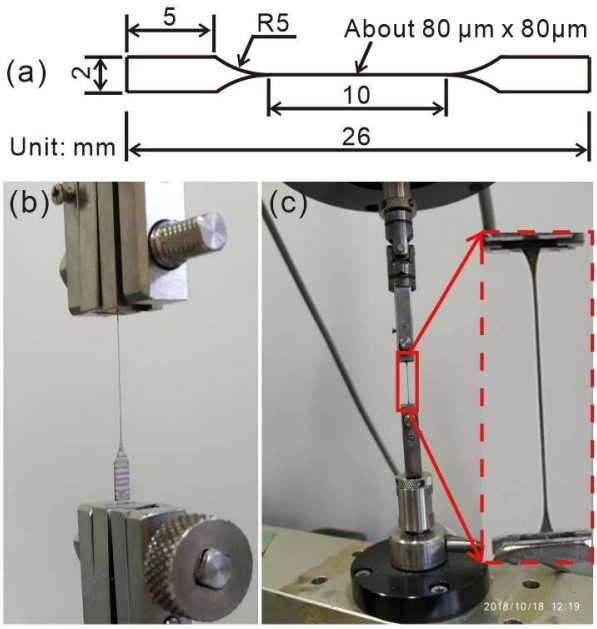

Fig. 1. The details of the slender tensile test. (a) The configuration of the slender tensile specimen. (b) The photo of the final specimen of the slender tensile test. (c) The photo of the slender tensile test.

2.3. Regular tensile and high-cycle fatigue tests

The regular tensile (RT) tests were conducted on a universal testing machine (model: Instron 5982) using plate tensile specimens, of which the dimensions configurations can be seen in Fig. 2a, at a strain rate of 5×10^{-4} s^{-1} at room temperature. Plate fatigue specimens (Fig. 2b) were machined from the aged bar, then electrolytically polished to remove any defects caused by machining. Because the specimens had shallow notches, the fatigue strength reduction factor for this geometry was close to 1. The HCF tests were conducted on an Instron 8801 test machine with a stress ratio of $R = -1$, and the frequency here was 30 Hz. The tensile and fatigue damage morphologies on the specimens and fractured surfaces were observed using SUPRA 35 SEM.

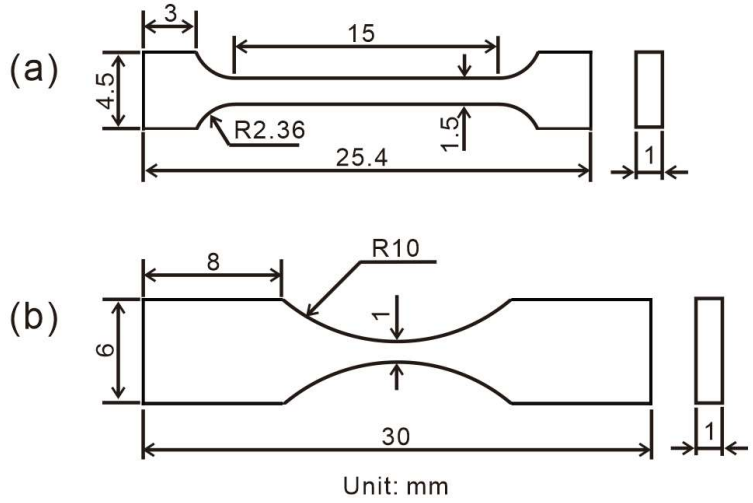

Fig. 2. The dimensions of specimens used for (a) regular tensile tests and (b) fatigue tests.

2.4. The fatigue strengths

In the present study, two fatigue strengths were obtained. One is the fatigue strength at the conditional life of 2×10^6 cycles. It was determined by the staircase method in which at least three pairs of specimens were tested. The other one is the fatigue strength at infinite life. It was acquired by fitting the data of the stress amplitude-cycles to failure curve using the Tanaka model [23], which will be introduced later.

3. Experimental results

3.1. Microstructure

It has been long known that the microstructure of 18Ni Co-free maraging steel is mainly lath martensite [4, 24-26] with rod-shaped precipitates [27]. The microstructures of the specimens under different aging treatments are revealed by the electropolishing. Because different phases and structures have different reaction rates, they have different surface topographies that can be summarized as precipitates, matrix, and boundary as shown in Fig. 3, respectively. The microstructure is approximate to the classic lath martensite structure [28, 29]: prior austenite grains are divided into packets, packets are subdivided into blocks, and blocks contain interleaved laths as schematically illustrated in Fig. 4a. During the aging treatment, the precipitates nucleate and grow up, and the reversion of the martensite matrix to austenite also occurs. The reverse austenite is caused by the segregation of nickel that is the austenite stabilizing solute at the lath boundary [24, 25]. As illustrated in Fig. 4b, in the meantime of the reversion of

martensite to austenite, the PFZ emerges due to the dissolution of the precipitates near the boundary [30], and the alloy rich austenite forms. With the change of aging treatment, the shape of the reverted austenite varies. As shown in Fig. 4c, when the aging temperature is 500 °C, the reverted austenite can only be seen along the lath boundary, while the aging temperature is relatively high, the reverted austenite exists in both inter-lath and intra-lath. It can be seen from Fig. 3c-d that the reverted austenite formed intra-lath is isolated from the lath boundary during the coarsening process and elongates parallel to the boundary until two of them converge.

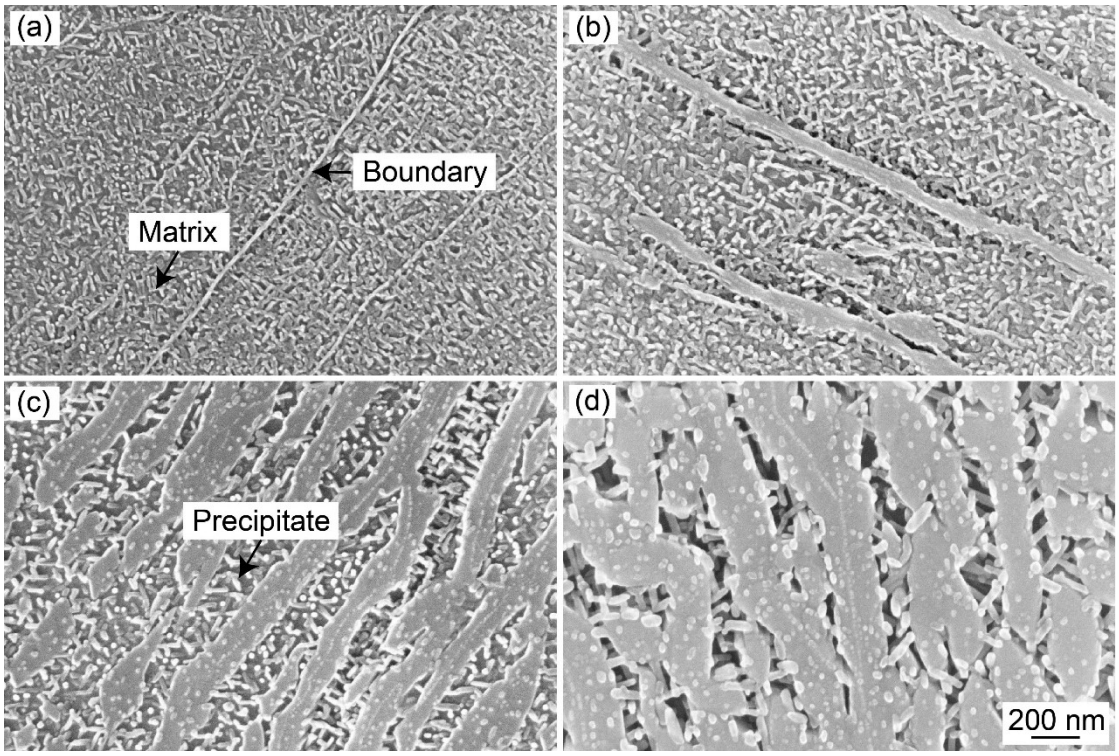

Fig. 3. The SEM images of microstructure for the 18Ni maraging steel aged at (a) 500 °C for 5 h, (b) 550 °C for 5 h, (c) 600 °C for 3 h, and (d) 630 °C for 3 h. The matrix with precipitates and strip-like boundaries can be recognized. All the images are in the same magnification.

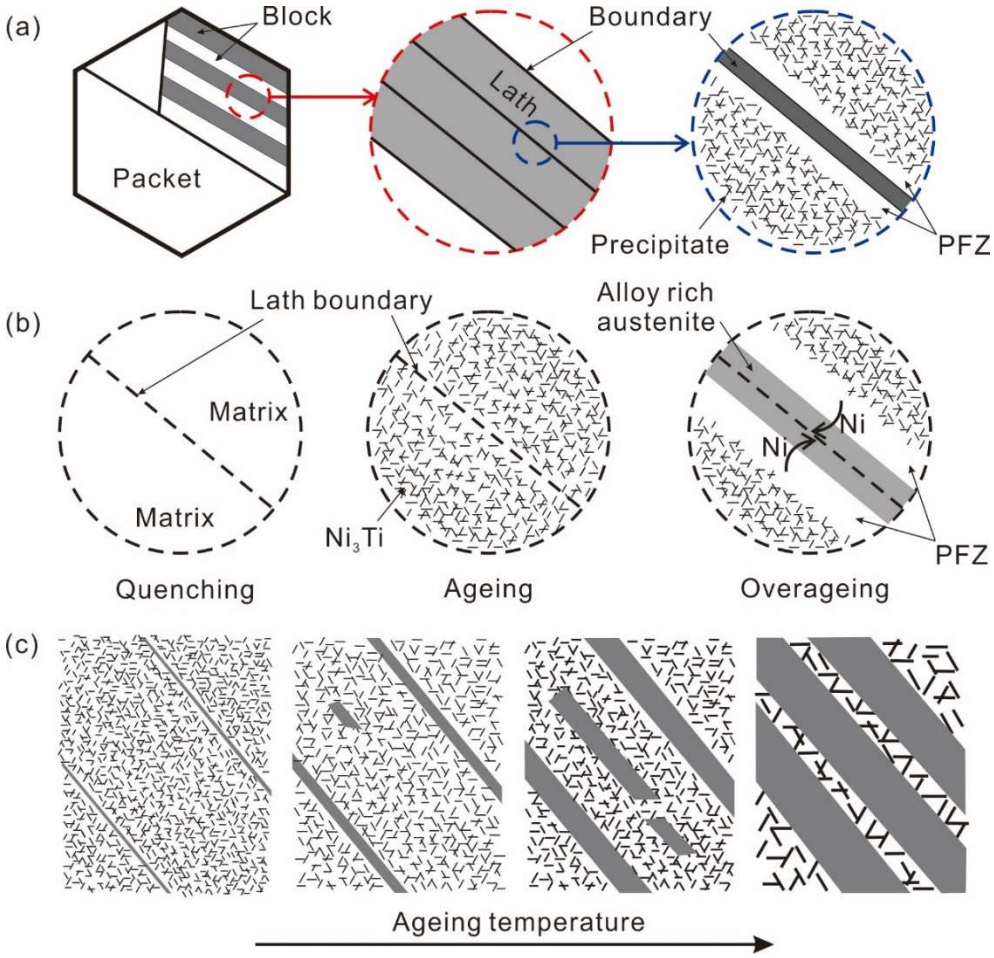

Fig. 4. Schematic illustration of microstructures for the 18Ni maraging steel. (a) The classic lath martensite structure. (b) The mechanism of austenite reversion in the present steel and the formation of the precipitate free zone (PFZ). (c) The schematic illustration of the evolution of the microstructures for the specimens under different aging treatments, e.g. 500 °C for 5 h, 550 °C for 5 h, 600 °C for 3 h and 630 °C for 3 h.

3.2. Tensile properties of regular and slender specimens

Fig. 5 presents the tensile stress-strain curves of RT and ST tests under different aging conditions. Typical effects of aging treatment and specimen size on UTS and yield strength (YS) can be seen in Table 2. Examination of the influences of aging and specimen dimension on tensile properties reveals some interesting features. Firstly, all the UTS and YS of the ST tests are lower than those of the RT tests under all aging conditions. Secondly, the uniform elongation of the ST test is less than that of the RT test under all aging conditions and there is almost no plastic elongation for the specimen aged at 500 °C for 5 h in the ST test. Thirdly, in the ST test the fracture occurs almost immediately after the stress reached the UTS point, while in the RT test there is a relatively high plastic strain between the UTS point and the fracture point.

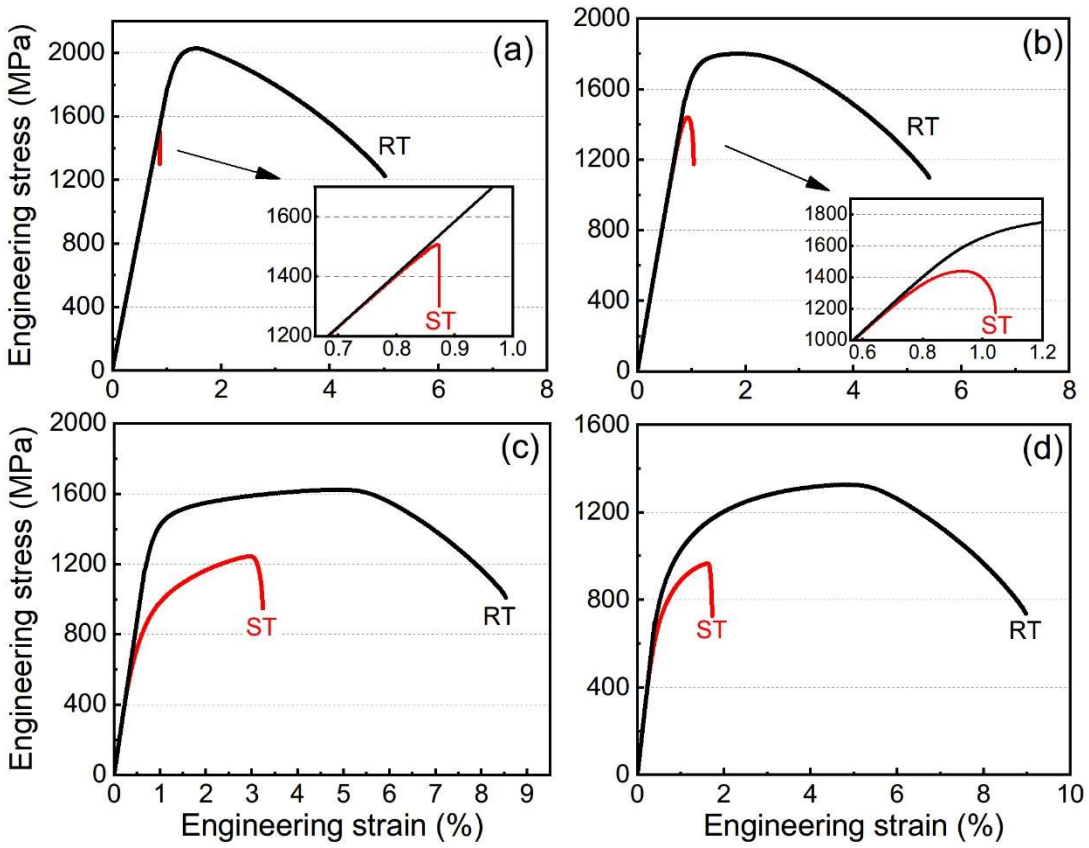

Fig. 5. Results of regular tensile (RT) and slender tensile (ST) tests of specimens under aging treatments of (a) 500 °C for 5 h, (b) 550 °C for 5 h, (c) 600 °C for 3 h, and (d) 630 °C for 3 h

Table 2. Tensile and fatigue properties of specimens aging at different temperatures.

Aging conditions	$\sigma_{UTS}^{RT}\ (MPa)$	$\sigma_{YS}^{RT}\ (MPa)$	$\sigma_{YS}^{ST}\ (MPa)$	$\sigma_{-1}^{C}\ (MPa)$	$\sigma_{-1}^{I}(MPa)$
500 °C for 5 h	1970 ± 17	1730 ± 15	(1440) [a]	698	688
550 °C for 5 h	1780 ± 23	1480 ± 36	(1140) [a]	665	660
600 °C for 3 h	1600 ± 25	1170 ± 7	560 ± 21	595	578
630 °C for 3 h	1340 ± 13	715 ± 11	540 ± 42	555	547

[a] Value of the sample with the smallest sectional area.

*σ_{UTS}^{RT} and σ_{YS}^{RT}: ultimate tensile strength and yield strength (0.01% offset) of the regular tensile test; σ_{YS}^{ST}: yield strength (0.01% offset) of the slender tensile test; σ_{-1}^{C}: fatigue strength at conditional life of 2×10^6 cycles (staircase method, $R=-1$) of the bulk material; σ_{-1}^{I}: fatigue strength at infinite life (fitting by the Tanaka model, $R=-1$).

Fig. 6 shows typical SEM images, depicting features of surfaces around the necking of the fractured specimens in the RT tests under different aging conditions. Although the mechanical properties vary for the specimens under four aging conditions there is an indication of the similar surface deformation bands (DBs) distributing throughout the grains or the pockets. Note that, at the aging treatments of 600 °C for 3 h and 630 °C for 3 h with similar elongation to failure of 8.0% and 8.5%, respectively, the surface DBs around the necking of the latter have less protuberance. The morphologies of surfaces away from the necking part of the fractured specimens are shown in Fig. 7. It is evident that there are relatively less DBs on the surfaces of specimens under 500 °C for 5 h and 550 °C for 5 h with uniform elongation of 0.3% and 0.9%, respectively, and much more under 600 °C for 3 h and 630 °C for 3 h with uniform elongation of 4.3% and 4.0%, respectively.

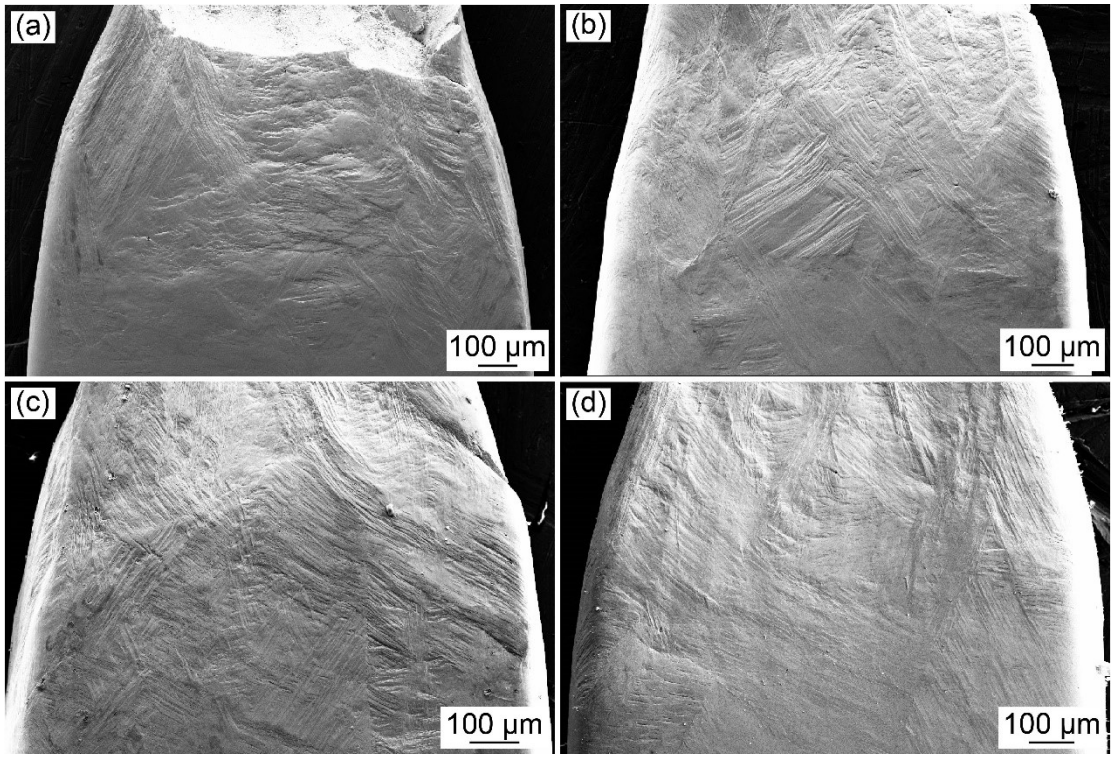

Fig. 6. The SEM images of the regular tensile specimens around the necking under aging conditions of (a) 500 °C for 5 h, (b) 550 °C for 5 h, (c) 600 °C for 3 h, and (d) 630 °C for 3 h.

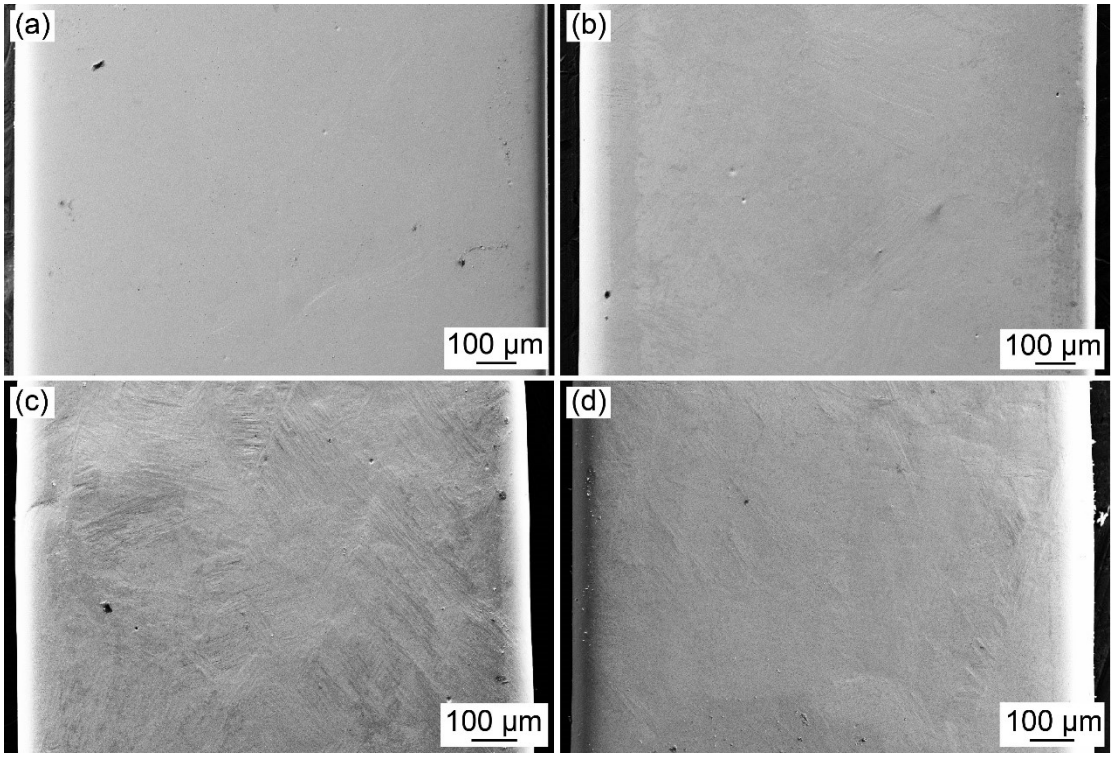

Fig. 7. The SEM images of the regular tensile specimens around the uniform elongation parts under aging conditions of (a) 500 °C for 5 h, (b) 550 °C for 5 h, (c) 600 °C for 3 h, and (d) 630 °C for 3 h.

Fig. 8 shows typical SEM images, revealing features of surface slip bands (SBs) of the ST specimens after failure under different aging conditions. On ST specimens aged at 500 °C for 5 h, there is barely necking with a flat shear fracture at an angle of about 50°. Figs. 7b-e reveal some interesting features. Firstly, when aged at 500 °C for 5 h and 550 °C for 5 h, there are some SBs within the lath, while for the specimens aged at 600 °C for 3 h and 630 °C for 3 h, there are still some SBs between the laths, to be more precise, along the PFZ. Secondly, when aged at 500 °C for 5 h and 550 °C for 5 h, the SBs are in large numbers, while each SB only bears a small amount of plastic deformation. However, when aged at 600 °C for 3 h and 630 °C for 3 h, there are only several local SBs on the specimen surface, while each of them undertakes a lot of plastic deformation so that some steps are formed. It should be noted that, the sectional area of the ST specimen is about 80×80 μm^2 that is smaller than the average grain or pocket size. Therefore, the plastic deformation is mainly concentrated in a preferred oriented pocket that is subjected to the maximum shear stress. And, there should be no plastic deformation outside that pocket.

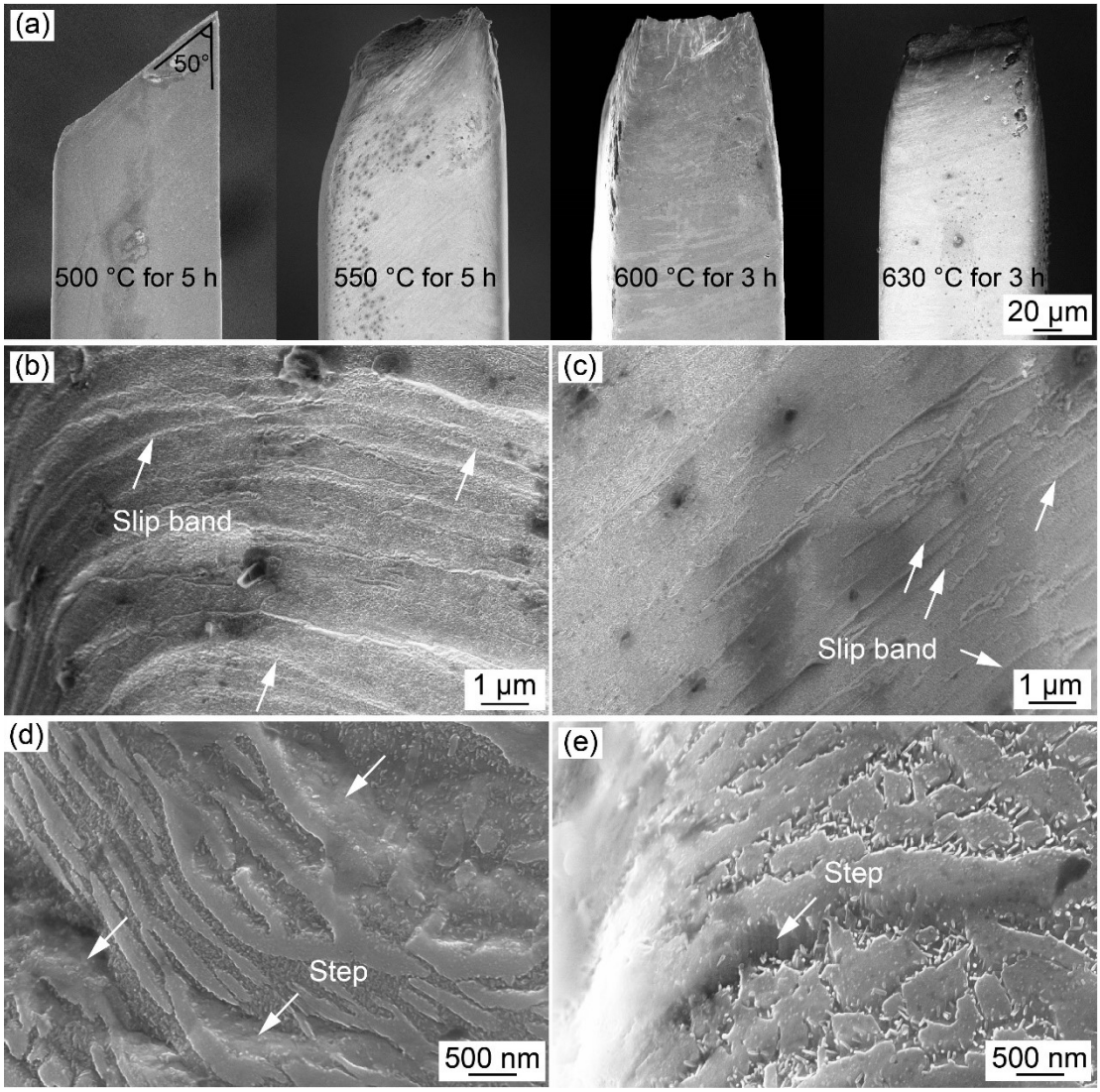

Fig. 8. The SEM images of the slender tensile specimens after failure (a) in macro views, and details under aging conditions of (b) 500 °C for 5 h, (c) 550 °C for 5 h, (d) 600 °C for 3 h, and (e) 630 °C for 3 h. The arrows mark the local deformation.

3.3. High-cycle fatigue behavior

Fig. 9 summarizes the results for correlation of the stress amplitude and the number of cycles to failure for the specimens under different aging conditions. It is obvious that for the four aging treatments the HCF strength enhances when the aging temperature decreases, i.e. the HCF strength improves as increasing the UTS. The fatigue strength staircase diagrams of the specimens under different aging treatments are displayed in Fig. 10. Compared to the results of Wang et al. [4], the fatigue strength of the unpolished specimens firstly improves as the UTS increases and then reduces dramatically. It can be confirmed that the surface roughness has a significant impact on

the fatigue strength for ultra-high strength steels.

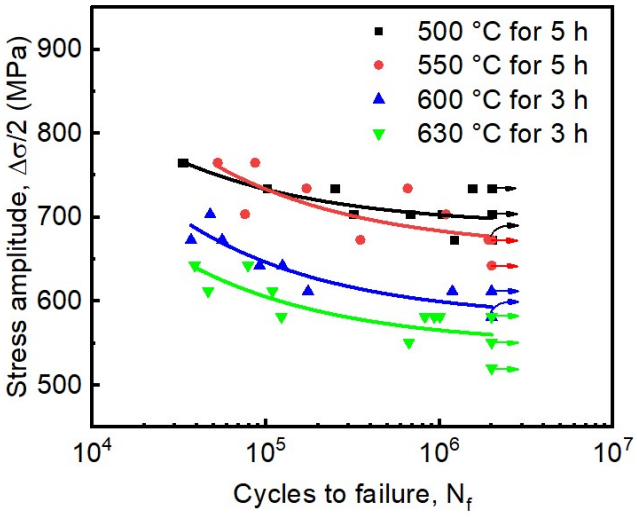

Fig. 9. The stress amplitude-number of cycles to failure curves for specimens under different aging treatments

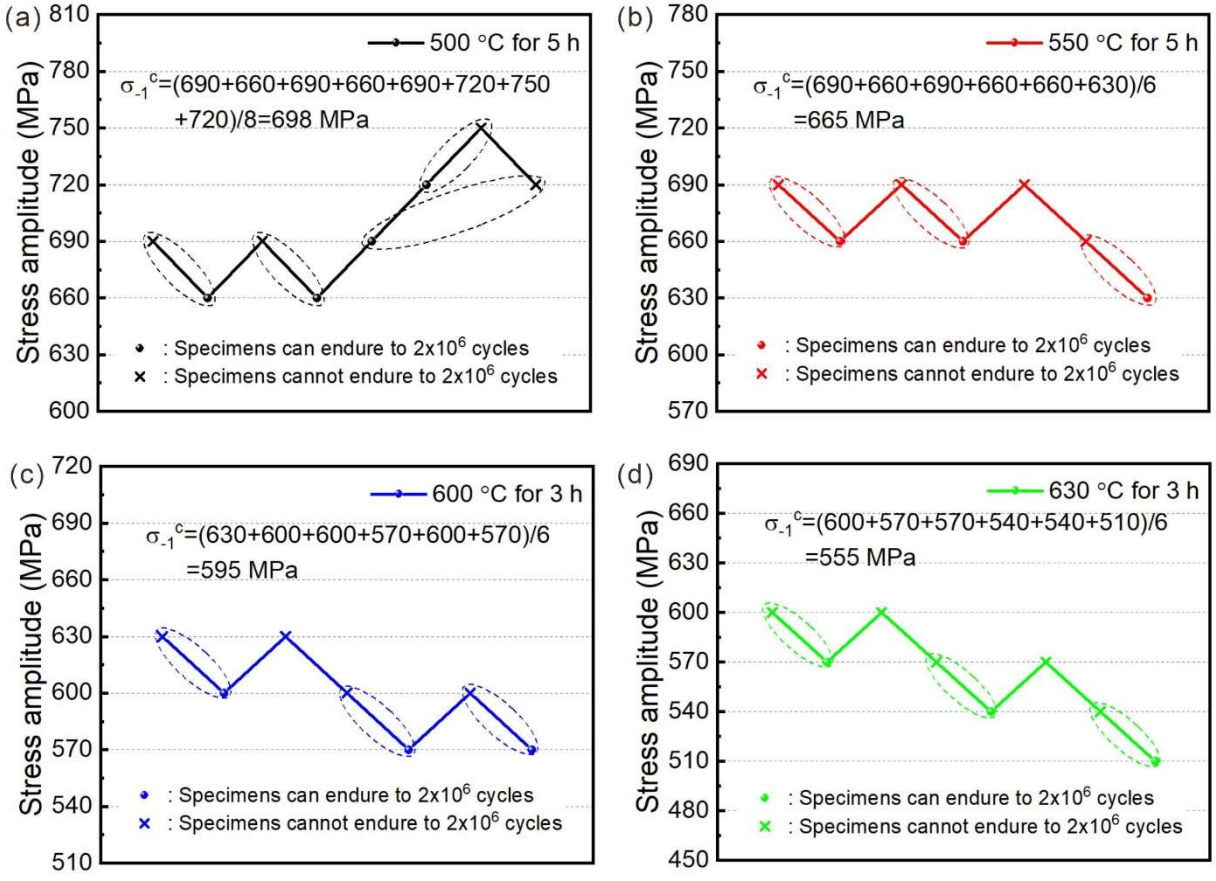

Fig. 10. The fatigue strength staircase diagrams of specimens under different aging treatments. (a) Aged at 500 °C for 5 h; (b) aged at 550 °C for 5 h; (c) aged at 600 °C for 3 h; (d) aged at 630 °C for 3 h.

Figs. 11-14 show typical SEM images revealing the features of fatigue crack

initiation sites of the fatigued specimens. For the specimen aged at 500 °C for 5 h, the macroscopic view of the fatigue crack initiation and growth are displayed in Figs. 11a-d. It can be seen that the fatigue crack initiated from the grain at the corner of the specimen and the details of the microstructure can be seen in Figs. 11e-f. It is apparent that the crack mainly initiated along the boundary of the lath and the angle between the lath and the load direction is about 45°, which is the case of the maximum shear stress. As shown in Fig. 11c, after initiating along the lath boundary, the crack branches when its length is about 50 μm in horizontal. The new branch is perpendicular to the loading direction. As for the original branch, it continues to grow for about 20 μm long in horizontal before ceasing. For the specimen aged at 550 °C for 5 h (Fig. 12), due to the boundary coarsening, it is evident that the crack grows inside the PFZ as shown in Fig. 12f. For those specimens aged at 550 °C for 5 h, 600 °C for 3 h, and 630 °C for 3 h the results are similar to those for the specimens aged at 500 °C for 5 h. It should be mentioned that there are no defects like inclusions, oxides, and voids in the fatigue crack initiation location. Thus, it may be the accumulation of irreversible strain in the PFZ that caused the fatigue crack initiation.

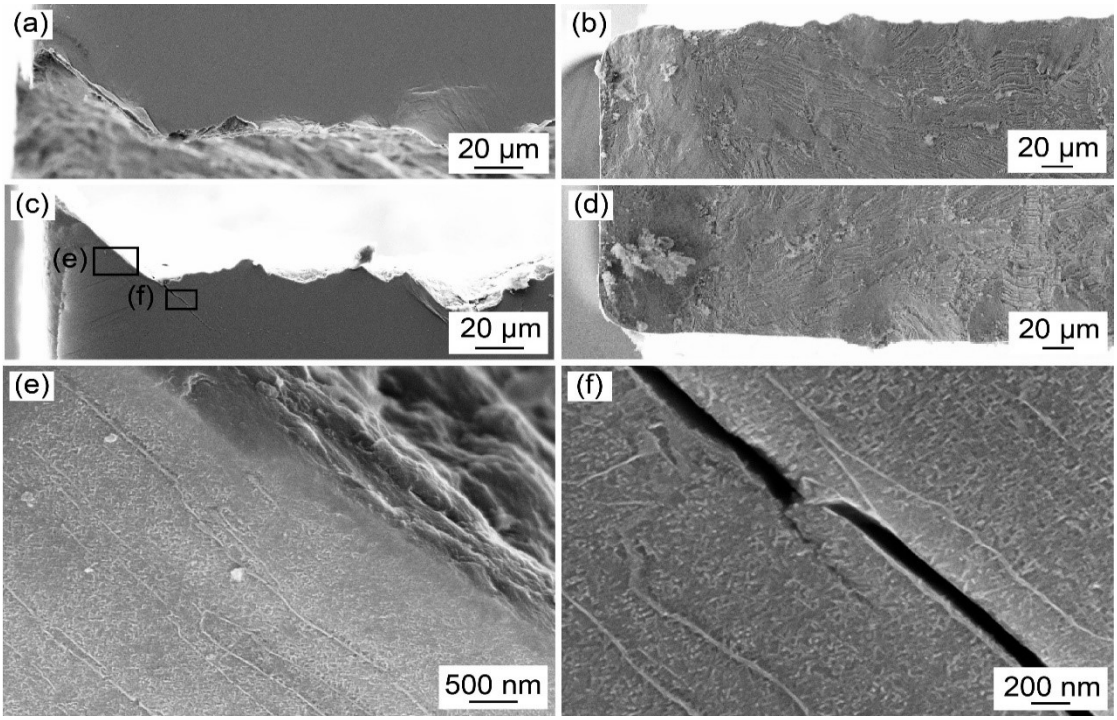

Fig. 11. The crack initiation location of specimen aged at 500 °C for 5 h. The side views (a) and (c) and the fractographies (b) and (d) of the crack initiation location. (e) and (f) The high magnification images of the places marked in (c).

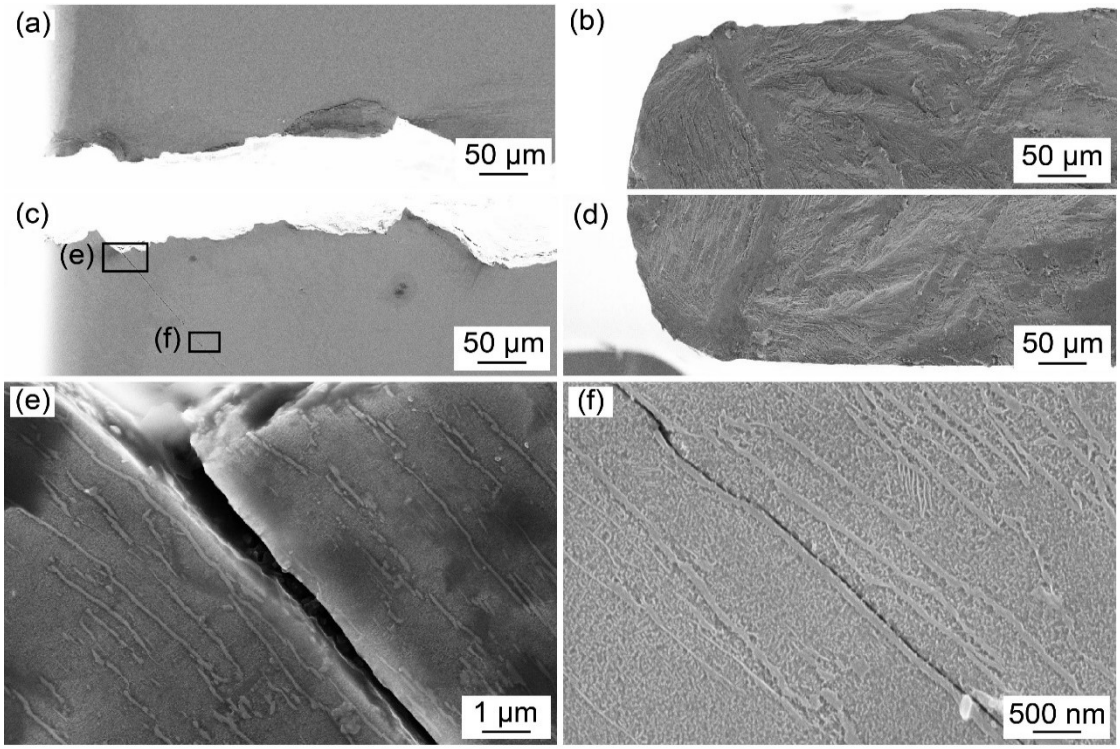

Fig. 12. The crack initiation location of specimen aged at 550 °C for 5 h. The side views (a) and (c) and the fractographies (b) and (d) of the crack initiation location. (e) and (f) The high magnification images of the places marked in (c).

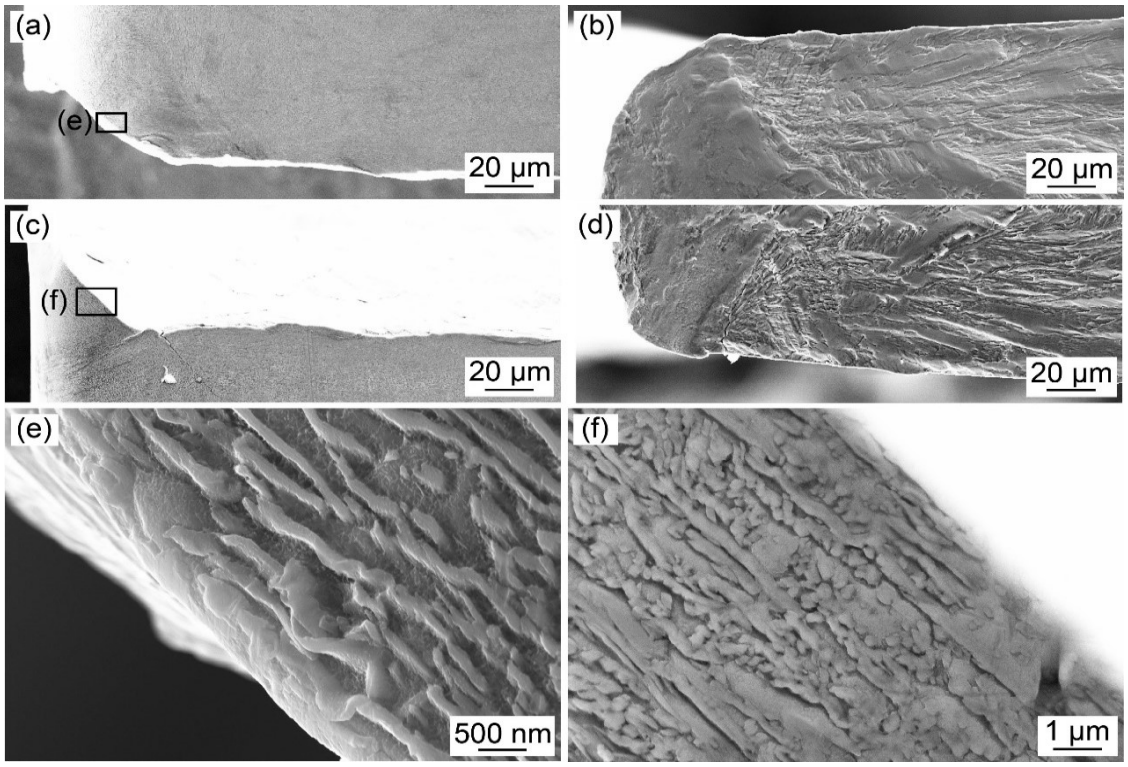

Fig. 13. The crack initiation location of specimen aged at 600 °C for 3 h. The side views (a) and (c) and the fractographies (b) and (d) of the crack initiation location. (e) and (f) The high magnification images of the places marked in (a) and (c).

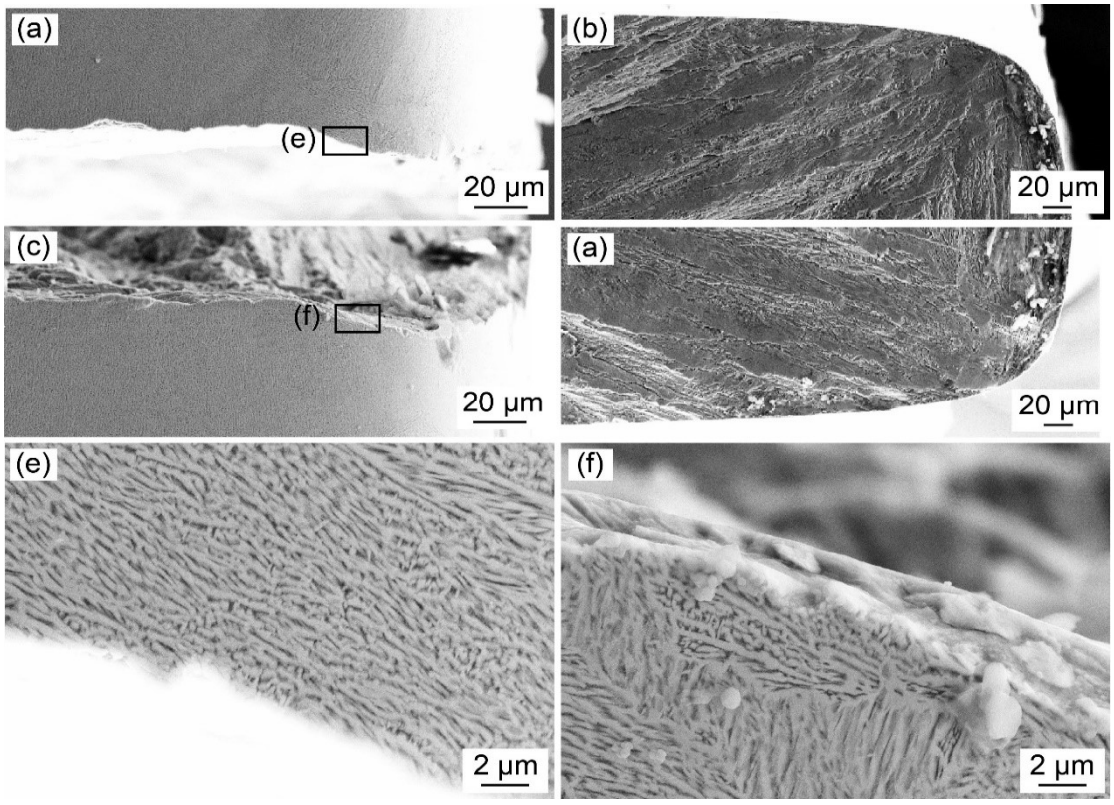

Fig. 14. The crack initiation location of specimen aged at 630 °C for 3 h. The side views (a) and (c) and the fractographies (b) and (d) of the crack initiation location. (e) and (f) The high magnification images of the places marked in (a) and (c).

Comparing the fracture morphologies of regular specimens subjected to the fatigue, RT and ST tests some similarities can be disclosed. Firstly, the PFZ is the weakest part of the microstructure for both the fatigue and tensile tests. Secondly, both the tensile and fatigue damages occur first on the oriented martensite lath that is subjected to the maximum shear stress. On the other hand, it is worth noting that when aging at 600 °C for 3 h and 630 °C for 3 h, the fatigue strengths are roughly equative to the YS of the ST.

4. Discussion

Based on the experimental results above, it is evident that the YS of the slender specimens is very close to the fatigue strength when aged at 600 °C for 3 h and 630 °C for 3 h. There might be an essential connection between the tensile test of the slender specimens and fatigue tests. To explain that connection and extend this relationship to the engineering application, the corresponding model and theory need to be built. The main idea is that both the ST and fatigue tests could reflect the strength of the PFZ, which is the soft domain. During the ST process, the soft domain will start the dislocation slip first to produce the plastic strain [22]. During the fatigue process, the soft domain will cause strain concentration, which is candidly related to the localization of fatigue damage [23, 31-34]. Furthermore, the fatigue strength is controlled by the critical stress for slip initiation (CSSI) in the soft domain [35]. As the bridge of tensile and fatigue properties, the effect of the PFZ will be discussed firstly.

4.1. Formation and weakness of precipitate-free zone

The main factors affecting the formation of PFZ in aging strengthening alloy should be solute and vacancy depletion [36, 37]. In the present steel, the concentration of Ni in the reverted austenite is considered to explain the occurrence of the PFZ [24]. The result of the EDS (Fig. 15) confirms the Ni concentration in the reverted austenite. Based on that, it is suspected that, due to the diffusion of Ni towards reverted austenite, a lamella shaped Ni depletion zone will form alongside the reverted austenite, thus the Ni_3Ti in that zone will dissolve, and the lamella shaped PFZ will subsequently occur as shown in Fig. 4a. According to the observation results in Figs. 8, 11-14, it can be concluded that the PFZ is the relatively soft domain in the microstructures of the present

steels because the surface steps as result of plastic deformation occurred in the PFZ under ST tests and the crack initiated in the PFZ under cyclic loading. Similar results in Ti and Al alloys were also reported by other researchers [18-20].

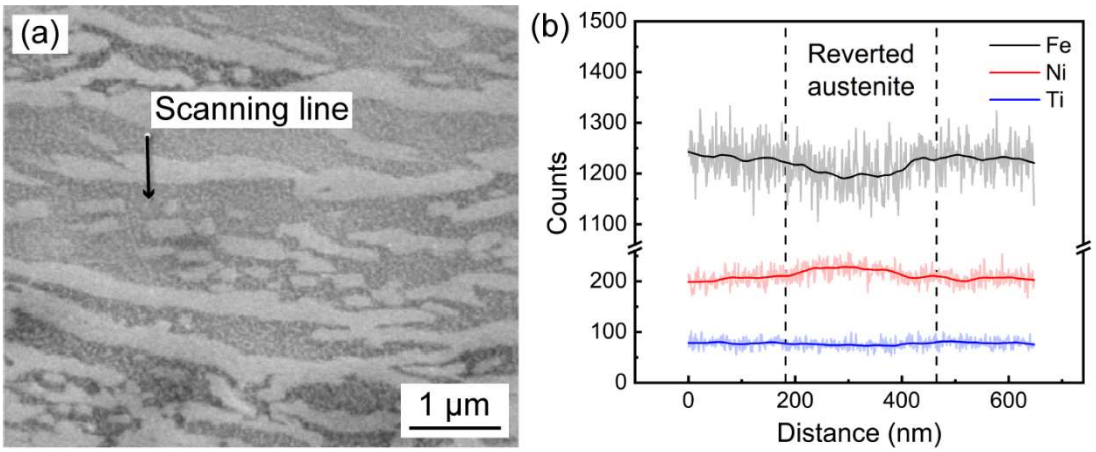

Fig. 15. The EDS results showing the concentration of Ni in the reverted austenite aging at 600 °C for 3 h. (a) The SEM image of the location of the scan line. (b) The EDS results.

4.2. Characteristics of the tensile test of slender specimens

The main difference between the ST and RT is that the sectional area of the ST is smaller than its average grain or pocket area. The average grain or pocket area in the present study is about 100×100 μm^2 and the sectional area of the ST specimens is intentionally shrunk to about 80×80 μm^2. By breaking through that critical sectional area, a single pocket will occupy the whole section for a short term as schematically illustrated in Fig. 16. Thus, significantly different tensile deformation behaviors for RT and ST specimens can be observed in the present Co-free maraging steel, which can be revealed by the elongation reduction and the early yielding.

4.2.1. Elongation reduction

The observed reduction in the elongation (Fig. 5) can be divided into uniform elongation (UE) and post-necking elongation by the necking point. The decline of UE is mainly caused by the absence of the extra hardening ability of polycrystalline materials. As shown in Fig. 16, for the RT, when the dislocation motion starts at the weakest oriented grain, the hard domain remains elastic, thus the yielding might not occur until the accumulative stress forces the dislocation motion in the neighbor hard

grain [22]. Therefore, the successive hardening of each grain produces a homogeneous distribution of strain and further a larger uniform elongation. As for the ST, there is no extra limitation for the weakest oriented grain so that it would sustain the most strain to the failure. That is to say, the reduction of UE happens only when the sectional area of the specimen is smaller than the average grain size. Otherwise, the specimen dimension has no evident influence on the uniform elongation, as reported by Zhao et al. [38], in which the grain/sub grain sizes are in the range of 100 nm – 1 μm and specimen thickness is greater than 250 μm. However, the specimen dimension indeed tends to have a significant effect on the post-necking elongation. It is been reported that the decrement of the post-necking elongation mainly originates from the strain definition [38]. That is to say, the post-necking strain is defined by the result of post-necking displacement divided by gauge dimension, thus, when the aspect ratio is as large as that of the ST in the present study the post-necking strain is negligible.

4.2.2. Early yielding

As for the early yielding phenomenon of the ST, before mechanism analysis, it is necessary to declare that the section of the ST specimens is about 80×80 μm^2, and it is much large than the critical value of the size effect caused by dislocation starvation [39]. The reasons for the early yielding might be attributed to two aspects. Firstly, the polycrystalline structure in the RT specimen could delay the yielding that should have occurred in the weakest oriented grain to the general yielding, while the single grain occupied section of the ST specimen would directly yield, as schematically illustrated in Fig. 16. All the materials with four different aging treatments may be affected by this aspect. It should be noted that, in the ST specimen, there might be often the case that single grain or pocket occupying the section occurs at different regions in one specimen, but only the weakest oriented grain or pocket will yield and determine the yield strength during the tensile test. Secondly, the attendance of the PFZ, which is the soft domain, might further reduce the yield strength.

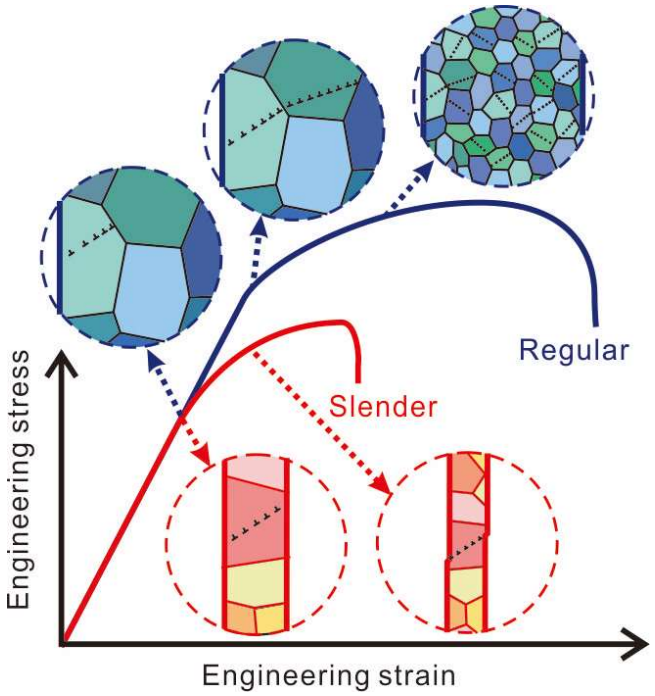

Fig. 16. Schematic illustration of the difference in specimen size during tensile tests between the regular and slender specimens, which affect their stress-strain curves.

4.2.3. Soft domain

The attendance of the soft domain might and might not further reduce the yield strength. The results need to be confirmed by the subsequent SEM observations on the fracture morphologies, as shown in Fig. 8. In order to better understand the deformation characteristics in Fig. 8, they are summarized as illustrated in Fig. 17. For those specimens aged at 500 °C for 5 h and 550 °C for 5 h, there are some SBs within the lath. The SBs are in large numbers, while each SB only bears a small amount of plastic deformation. That is to say, the soft domain around LB cannot deform freely and the measured yield strength is the weakest oriented grain, not the soft domain. For those aged at 600 °C for 3 h and 630 °C for 3 h, there are some SBs between the lath, to be more precise, along the PFZ. There are only several local SBs, while each of them undertakes a lot of plastic deformation so that the step is formed. In other words, the soft domain can deform freely, and the measured yield strength is of the soft domain.

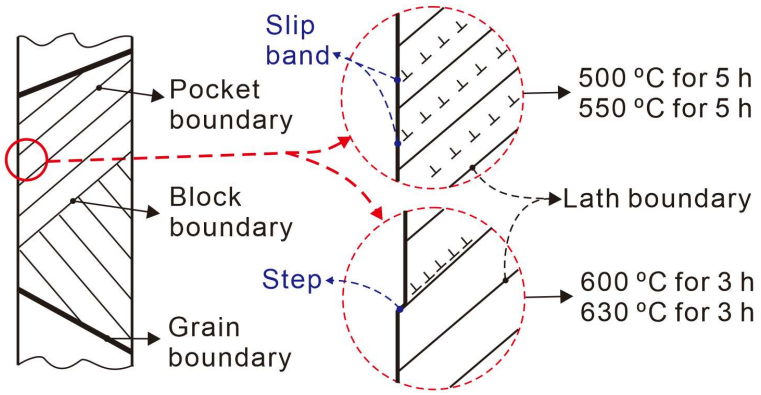

Fig. 17. Schematic illustration of the difference between two kinds of tensile deformation characteristics summarized from Fig. 8.

By the combination of the above analysis and the SEM images in Fig. 8, it is feasible to conclude that the ST tests of the specimens aged at 600 °C for 3 h and 630 °C for 3 h reveal the yield strength of the PFZ, while that of 500 °C for 5 h and 550 °C for 5 h do not.

4.3. Characteristics of fatigue strength

The fatigue strength listed in Table 2 was obtained by the staircase method, which is the fatigue strength at a conditional lifetime (2×10^6). On the other hand, according to the dislocation model for fatigue crack initiation [23, 31-34], the material without metallurgical defects has a fatigue strength at infinite life cycles determined by the CSSI.

4.3.1. Fatigue strength at infinite life cycles

According to the Tanaka model [23], the simplified form of the model can be given as follows:

$$N_i = \frac{AW_s}{(\sigma_a - \sigma_{cr})^2}, \tag{1}$$

where N_i is the number of cycles to fatigue crack initiation, the value of W_s is the specific fracture energy for a unit area, σ_a is the stress amplitude, σ_{cr} is the uniaxial tensile stress corresponding to the CSSI, and A is a constant depending on the material properties. Furthermore, it can be written as:

$$\sigma_a = \sigma_{cr} + AW_s/\sqrt{N_i}. \tag{2}$$

The N_i is replaced by N_f since the fatigue crack initiation occupied the most of the total HCF life [40]. By fitting the data plotted in Fig. 9 using Eq. (2), the σ_a-N_f

curves of the specimens aged at 500 °C for 5 h, 550 °C for 5 h, 600 °C for 3 h, and 630 °C for 3 h are expressed as follows, respectively:

$$\sigma_a = 688 + 14114/\sqrt{N_f}, \quad (3)$$

$$\sigma_a = 660 + 23002/\sqrt{N_f}, \quad (4)$$

$$\sigma_a = 578 + 21680/\sqrt{N_f}, \quad (5)$$

$$\sigma_a = 547 + 18458/\sqrt{N_f}. \quad (6)$$

The fatigue strengths at infinite life cycles are listed in Table 2.

4.3.2. The fatigue strength

The above two kinds of fatigue strengths were obtained by different methods. In the view of the Tanaka model, the fatigue strength determined by the staircase method is higher than that determined by the CSSI because of the conditional lifetime feature. This conclusion could be supported by Eq. (2). More specifically, when N_i in Eq. (2) is a finite value, $AW_s/\sqrt{N_i}$ is larger than zero. Therefore, it is clear that the fatigue strength at infinite life cycles is the one that equal to the CSSI, so it should be the one to be compared with the yield strength of the ST.

4.4. Bridging the slender tensile and fatigue properties

Based on the above analyses, two conclusions can be drawn. Firstly, the local yield strength of the PFZ could be obtained by the tensile test of the slender specimens. Secondly, the fatigue strength of the bulk material could be considered as the CSSI in the PFZ. Assuming that the CSSI of the PFZ in the bulk material equals to that in the slender specimen, the fatigue strength of the bulk material should be the same as the local yield strength of the slender specimen. This is the only and essential assumption in the present theory that the fatigue strength of metals could be ascertained by the ST. Table 3 shows the ST and fatigue results of 600 °C for 3 h and 630 °C for 3 h supporting this assumption. As for 500 °C for 5h and 550 °C for 5h, the ST tests fail to obtain the yield strength of the soft domain. It is believed that some thinner tensile specimens are required to make the soft domain deform freely and methods other than the tensile test are needed to be developed.

Table 3. Comparison between the yield strength of slender specimens and fatigue strength of bulk specimens.

Aging treatment	Yield strength, σ_{YS}^{ST} (MPa)	Fatigue strength, σ_{-1}^{I} (MPa)
600°C for 3 h	560 ± 21	578 ± 10
630°C for 3 h	540 ± 42	547 ± 11

As a supplement, the identity of the damage distribution conditions between ST and fatigue could give an insight into the present theory. It is well known that the fatigue damage could be highly concentrated, thus the initiation of the fatigue crack is limited in one particular grain in general, and this particular grain is chosen because it has the lowest strength among all the grains [12]. Things are the same for the ST, and the weakest grain will yield first as long as the ST specimen size is appropriate. Therefore, the CSSI in the soft domain could be treated as the connection to bridge the tensile and fatigue properties.

5. Conclusions

Based on the experimental results of 18Ni maraging steels (250 grade) under different aging treatments, the relationship between fatigue and tensile properties is systematically discussed and analyzed, and the following conclusions can be drawn:

(1) The relatively low fatigue strength of the present steels is imputed to the attendance of the PFZ, which is caused by the segregation of Ni during the aging treatment. The fatigue strength is determined by the strength of the soft domain.

(2) The abnormal behaviors of slender tensile tests, including the elongation reduction and the early yielding, can be attributed to that a single grain or packet occupies the whole section of the specimen. In another words, the section area of the specimen is less than the grain size. In the present study, the PFZ, which is the soft domain, also contributes to the early yielding.

(3) The equation between the fatigue strength of bulk specimen and the yield strength of the slender specimen can be attributed to that the damage mechanism in the two types of tests is identical: the weakest grain will start the dislocation motion first. As long as the validity of the yield strength obtained by the tensile test of the slender

specimen can be guaranteed, the fatigue strength at infinite life cycles should be predictable for slip bands cracking metals by using the slender tensile test.

Credit author statement

Zikuang Xu: Conceptualization, Methodology, Formal analysis, Investigation, Data curation, Writing – original draft. **Bin Wang:** Resources, Writing – review & editing. **Peng Zhang:** Conceptualization, Formal analysis, Supervision, Writing – review & editing. **Zhefeng Zhang:** Supervision, Writing – review & editing.

Declaration of interest statement

The authors declare that they have no known competing financial interests or personal relationships that could have appeared to influence the work reported in this paper.

Acknowledgments

This work was financially supported by the National Natural Science Foundation of China (NSFC) under Grant Nos. 51771208 and U1664253, the Strategic Priority Research Program of the Chinese Academy of Sciences under Grant No. XDB22020202 and the LiaoNing Revitalization Talents Program under Grant No. XLYC1808027.

Data Availability

Data will be made available on request.

References

[1] L. Tóth, S.Y. Yarema, Formation of the science of fatigue of metals. Part 1. 1825–1870, Mater. Sci. 42(5) (2006) 673-680.

[2] J.C. Pang, S.X. Li, Z.G. Wang, Z.F. Zhang, General relation between tensile strength and fatigue strength of metallic materials, Mater. Sci. Eng. A 564 (2013) 331-341.

[3] B. Wang, P. Zhang, R. Liu, Q.Q. Duan, Z.J. Zhang, X.W. Li, Z.F. Zhang, An optimization criterion for fatigue strength of metallic materials, Mater. Sci. Eng. A 736 (2018) 105-110.

[4] B. Wang, P. Zhang, Q.Q. Duan, Z.J. Zhang, H.J. Yang, X.W. Li, Z.F. Zhang, Optimizing the fatigue strength of 18Ni maraging steel through ageing treatment,

Mater. Sci. Eng. A 707 (2017) 674-688.

[5] S. Suresh, Fatigue of Materials, 2 ed., Cambridge University Press, Cambridge, 1998.

[6] H. Mughrabi, Cyclic slip irreversibilities and the evolution of fatigue damage, Metall. Mater. Trans. A 40(6) (2009) 1257-1279.

[7] M.E. Fine, Fatigue resistance of metals, Metall. Trans. A 11(3) (1980) 365-379.

[8] Y. Murakami, Metal fatigue: effects of Small Defects and Nonmetallic Inclusions, 1st ed., Elsevier, Oxford, 2002.

[9] K.S. Chan, Roles of microstructure in fatigue crack initiation, Int. J. Fatigue 32(9) (2010) 1428-1447.

[10] Z.G. Wang, S.H. Ai, Fatigue of martensite-ferrite high strength low-alloy dual phase steels, ISIJ Int. 39(8) (1999) 747-759.

[11] E. Schmid, W. Boas, Plasticity of crystals, Chapman & Hall, London, 1935.

[12] R. Liu, Y.Z. Tian, Z.J. Zhang, P. Zhang, Z.F. Zhang, Fatigue strength plateau induced by microstructure inhomogeneity, Mater. Sci. Eng. A 702 (2017) 259-264.

[13] E.O. Hall, The deformation and ageing of mild steel: III discussion of results, Proc. Phys. Soc. 64(9) (1951) 747-753.

[14] N.J. Petch, The cleavage strength of polycrystals, J. Iron Steel Inst. Jpn. 174(1) (1953) 25-28.

[15] M. Okayasu, K. Sato, M. Mizuno, D. Hwang, D. Shin, Fatigue properties of ultra-fine grained dual phase ferrite/martensite low carbon steel, Int. J. Fatigue 30(8) (2008) 1358-1365.

[16] W. Zhongguang, W. Guonan, K. Wei, H. Haicai, Influence of the martensite content on the fatigue behaviour of a dual-phase steel, Mater. Sci. Eng. 91 (1987) 39-44.

[17] C.J. Szczepanski, S.K. Jha, J.M. Larsen, J.W. Jones, Microstructural influences on very-high-cycle fatigue-crack initiation in Ti-6246, Metall. Mater. Trans. A 39(12) (2008) 2841-2851.

[18] C. Huang, Y. Zhao, S. Xin, C. Tan, W. Zhou, Q. Li, W. Zeng, High cycle fatigue behavior of Ti–5Al–5Mo–5V–3Cr–1Zr titanium alloy with lamellar

microstructure, Mater. Sci. Eng. A 682 (2017) 107-116.

[19] C. Huang, Y. Zhao, S. Xin, C. Tan, W. Zhou, Q. Li, W. Zeng, Effect of microstructure on high cycle fatigue behavior of Ti–5Al–5Mo–5V–3Cr–1Zr titanium alloy, Int. J. Fatigue 94 (2017) 30-40.

[20] G. Lütjering, J. Albrecht, C. Sauer, T. Krull, The influence of soft, precipitate-free zones at grain boundaries in Ti and Al alloys on their fatigue and fracture behavior, Mater. Sci. Eng. A 468-470 (2007) 201-209.

[21] R. Liu, Y.Z. Tian, Z.J. Zhang, P. Zhang, X.H. An, Z.F. Zhang, Exploring the fatigue strength improvement of Cu-Al alloys, Acta Materialia 144 (2018) 613-626.

[22] X. Wu, Y. Zhu, Heterogeneous materials: a new class of materials with unprecedented mechanical properties, Mater. Res. Lett. 5(8) (2017) 527-532.

[23] K. Tanaka, T. Mura, A dislocation model for fatigue crack initiation, J. Appl. Mech. 48(1) (1981) 97-103.

[24] P.P. Sinha, D. Sivakumar, N.S. Babu, K.T. Tharian, A. Natarajan, Austenite reversion in 18 Ni Co-free maraging steel, Steel Res. 66(11) (1995) 490-494.

[25] P.P. Sinha, K.T. Tharian, K. Sreekumar, K.V. Nagarajan, D.S. Sarma, Effect of aging on microstructure and mechanical properties of cobalt free 18%Ni (250 grade) maraging steel, Mater. Sci. Technol. 14(1) (2013) 1-9.

[26] S. Morito, X. Huang, T. Furuhara, T. Maki, N. Hansen, The morphology and crystallography of lath martensite in alloy steels, Acta Mater. 54(19) (2006) 5323-5331.

[27] V.K. Vasudevan, S.J. Kim, C.M. Wayman, Precipitation reactions and strengthening behavior in 18 Wt Pct nickel maraging steels, Metall. Trans. A 21(10) (1990) 2655-2668.

[28] J.W. Morris, Jr., C. Kinney, K. Pytlewski, Y. Adachi, Microstructure and cleavage in lath martensitic steels, Sci. Technol. Adv. Mater. 14(1) (2013) 014208.

[29] S. Morito, H. Tanaka, R. Konishi, T. Furuhara, T. Maki, The morphology and crystallography of lath martensite in Fe-C alloys, Acta Mater. 51(6) (2003) 1789-1799.

[30] Y. He, K. Yang, W. Sha, Microstructure and mechanical properties of a 2000 MPa

grade co-free maraging steel, Metall. Mater. Trans. A 36(9) (2005) 2273-2287.

[31] M.R. Lin, M.E. Fine, T. Mura, Fatigue crack initiation on slip bands: Theory and experiment, Acta Metall. 34(4) (1986) 619-628.

[32] T. Mura, Y. Nakasone, A theory of fatigue crack initiation in solids, J. Appl. Mech.-Trans. ASME 57(1) (1990) 1-6.

[33] K.S. Chan, A microstructure-based fatigue-crack-initiation model, Metall. Mater. Trans. A 34(1) (2003) 43-58.

[34] M.D. Sangid, The physics of fatigue crack initiation, Int. J. Fatigue 57 (2013) 58-72.

[35] H. Mughrabi, The cyclic hardening and saturation behaviour of copper single crystals, Mater. Sci. Eng. 33(2) (1978) 207-223.

[36] P.N.T. Unwin, G.W. Lorimer, R.B. Nicholson, Origin of grain boundary precipitate free zone, Acta Metall. 17(11) (1969) 1363-1377.

[37] J.D. Embury, R.B. Nicholson, The nucleation of precipitates: The system Al-Zn-Mg, Acta Metall. 13(4) (1965) 403-417.

[38] Y.H. Zhao, Y.Z. Guo, Q. Wei, A.M. Dangelewiez, Y.T. Zhu, T.G. Langdon, Y.Z. Zhou, E.J. Lavernia, C. Xu, Influence of specimen dimensions on the tensile behavior of ultrafine-grained Cu, Scr. Mater. 59(6) (2008) 627-630.

[39] J.R. Greer, W.D. Nix, Nanoscale gold pillars strengthened through dislocation starvation, Phys. Rev. B 73(24) (2006).

[40] X.L. Zheng, On some basic problems of fatigue research in engineering, Int. J. Fatigue 23(9) (2001) 751-766.